MULTISCALE MODEL. SIMUL.
Vol. 20, No. 3, pp. 1147-1166

ADAPTIVE SOLUTION OF INITIAL VALUE PROBLEMS BY A DYNAMICAL GALERKIN SCHEME*

RODRIGO M. PEREIRA†, NATACHA NGUYEN VAN YEN‡, KAI SCHNEIDER§, AND MARIE FARGE¶

Abstract. Adaptive Galerkin methods for time-dependent partial differential equations are studied and shown to be dissipative. The adaptation implies that the subset of the selected basis function changes over time according to the evolution of the solution. The corresponding projection operator is thus time-dependent and nondifferentiable. We therefore propose to use an integral formulation in time. We analyze the existence and uniqueness of this weak form of the dynamical Galerkin scheme, and we then prove that the nonsmooth projection operator introduces energy dissipation, which is a crucial result for adaptive Galerkin methods, e.g., adaptive wavelet methods. Numerical examples for the inviscid Burgers equation in one dimension and the incompressible Euler equations in two and three spatial dimensions show that the selection of basis functions, for instance by filtering out weak wavelet coefficients from the solution, introduces energy dissipation. Moreover, for the Burgers case we can show that adaptive wavelet regularization yields convergence of the truncated Galerkin solution to the physically relevant entropy solution. These results motivate adaptive wavelet-based Galerkin schemes for nonlinear hyperbolic conservation laws.

Key words. wavelets, adaptivity, Galerkin method, dissipation

MSC codes. 65N30, 65N50, 65T60, 65M60

DOI. 10.1137/21M1459782

1. Introduction.

Motivated by achieving high accuracy at reduced computational cost compared to uniform grid methods, numerous adaptive discretization schemes of evolutionary partial differential equations (PDEs) have been developed for decades; see, e.g., [6]. Real-world problems, for instance fluid and plasma turbulence or reactive flows, typically involve a multitude of active spatial and temporal scales, while adaptivity allows us to concentrate the computational effort at locations and time instants where it is necessary to ensure a given numerical accuracy, whereas elsewhere efforts may be significantly reduced. Among adaptive approaches, multiresolution and wavelet methods offer an attractive possibility to introduce locally refined grids, which dynamically track the evolution of the solution in space and scale. Automatic error control of the adaptive discretization, with respect to a uniform grid solution, is hereby an advantageous feature [9]. For a review of adaptive

* Received by the editors November 16, 2021; accepted for publication (in revised form) March 31, 2022; published electronically September 30, 2022.
https://doi.org/10.1137/21M1459782
Funding: This research was supported by the French Federation for Fusion Studies and the PEPS program of CNRS-INSMI. This work, supported by the European Communities under the contract of Association between EURATOM, CEA, and the French Research Federation for Fusion Studies, was carried out within the framework of the European Fusion Development Agreement. The views and opinions expressed herein do not necessarily reflect those of the European Commission.

† Instituto de Física, Universidade Federal Fluminense, Niterói, 24210-346, Brazil (rodrigomp@id.uff.br).

‡ LMD-CNRS, École Normale Supérieure-PSL, 75230, Paris, Cedex 05, France, and FB Mathematik und Informatik, Freie Universität Berlin, Berlin, Germany (rnguyen@zedat.fu-berlin.de).

§ Institut de Mathématiques de Marseille (I2M), CNRS, Aix-Marseille Université, Marseille, 13453, France (kai.schneider@univ-amu.fr).

¶ LMD-CNRS, École Normale Supérieure-PSL, 75230, Paris, Cedex 05, France (marie.farge@ens.fr).

multiresolution methods in the context of computational fluid dynamics (CFD) we refer the reader to [36].

In many applications, in particular in CFD, Galerkin truncated discretizations of the underlying PDEs, which use a finite number of modes, are the methods of choice. Spectral methods [7] are a prominent example, and Fourier–Galerkin schemes are widely used for direct numerical simulation of turbulence [20] due to their high accuracy. For efficiency reasons, the convolution product in spectral space, due to the nonlinear quadratic term and typically encountered in hydrodynamic equations, is evaluated in physical space, and aliasing errors are completely removed. This implementation, called pseudo-spectral formulation with full dealiasing using the 2/3 rule, is equivalent to a Fourier–Galerkin scheme up to round-off errors [7]. Thus the discretization conserves the L^2-norm of the solution. A classical test to check the stability of pseudo-spectral codes for viscous Burgers or Navier–Stokes equations is to perform simulations with vanishing viscosity. This allows us to verify whether the L^2-norm of the solution, i.e., typically energy, is conserved and for sufficiently small time steps the truncated Galerkin schemes are stable. However, the solution of the Galerkin truncated inviscid equations, e.g., inviscid Burgers or incompressible Euler, shows a peculiar behavior in the form of oscillations, and the computed solution is not physical. Although remarkable, this behavior is not completely unexpected. Already T.D. Lee [23] predicted energy equipartition between all Fourier coefficients in spectral approximations for 3D incompressible Euler, called thermalization, by applying Liouville's theorem from statistical mechanics.

The effect of truncating Fourier–Galerkin schemes has been studied in [24] for the 1D Burgers equation and in [8] for the 3D incompressible Euler equation. Later, detailed numerical studies were carried out in [34] for both the Burgers and the 2D incompressible Euler equations. The observed short-wavelength oscillations were named "tygers" and were interpreted as the first manifestations of thermalization [23]. The proposed cause was the resonant interaction between fluid particle motion and truncation waves. Tyger purging was then proposed in [26] using selective removal of a narrow boundary layer in Fourier space, close to the truncation wavenumber at discrete time intervals.

Motivated by previous work, detailed numerical analysis of Fourier–Galerkin methods for nonlinear evolutionary PDEs, in particular for inviscid Burgers and incompressible Euler, was then performed in [4]. The authors showed spectral convergence for smooth solutions of the inviscid Burgers equation and the incompressible Euler equations. However, when the solution lacks sufficient smoothness, then both the spectral and the 2/3 pseudo-spectral Fourier methods exhibit nonlinear instabilities, which generate spurious oscillations. In particular, it was shown that after the shock formation in the inviscid Burgers equation, the total variation of bounded (pseudo-) spectral Fourier solutions must increase with the number of increasing modes. The L^2-energy conservation of the spectral solution is reflected through spurious oscillations, which is in contrast with energy dissipating Onsager solutions. A complete explanation of these nonlinear instabilities was thus given, and "tygers" [34] were demystified.

These issues are closely related to what is known in the turbulence literature as the dissipative anomaly, which is the fact that time reversal symmetry is not restored in the limit where the symmetry breaking parameter, i.e., viscosity, goes to zero. To reproduce the expected dissipative behavior in truncated Galerkin approximations, these unphysical oscillations must be removed. For this purpose different numerical regularization techniques have been proposed, which are commonly used in numerical

methods for solving hyperbolic conservation laws. If the solution is not unique, the "regularized" numerical scheme selects one weak solution, which should correspond to the physically relevant one, e.g., the entropy solution of the inviscid Burgers equation, which can be computed exactly using the Legendre transform [40]. These approaches include upwind techniques [31], total variation diminishing schemes [19], shock limiters [38], spectral vanishing viscosity [39, 18], inviscid regularization schemes [3, 22], and classical viscosity and hyperviscosity [5]. In the case of hyperviscosity it has been shown [16, 2] that, for sufficiently high powers of the Laplacian in the dissipative term, the unregularized conservative dynamics is recovered, while for moderate powers a bottleneck effect occurs in the energy-spectrum [17]. Recently, a method based on the suppression of a narrow band of Fourier modes at discrete time-intervals has been proposed in [26], and the resulting solution shows numerical convergence to the entropy solution as the spatial resolution increases. This method, which has almost no additional computational cost, can be viewed as a periodic filtering in Fourier space, where the Galerkin projection space changes discontinuously at regular time intervals. These discontinuous changes in the projection operators are precisely the type of situation we seek to formalize here, but on more general grounds, taking into account other possible projection bases.

In the context of adaptive wavelet schemes, numerical experiments with the 1D inviscid Burgers equation showed that wavelet filtering of the Fourier–Galerkin truncated solution in each time step, which corresponds to denoising and is removing the oscillations, yields the solution to the viscous Burgers equation [27]. For the 2D incompressible Euler equations [28] different wavelet techniques for regularizing truncated Fourier–Galerkin solutions were studied using either real-valued or complex-valued wavelets, and the results were compared with viscous and hyperviscous regularization methods. The results show that nonlinear wavelet filtering with complex-valued wavelets preserves the flow dynamics and suggests L^2 convergence to the reference solution. The wavelet representation offers at the same time a non-negligible compression rate of about 3 for fully developed 2D turbulence.

Simulations of the 3D wavelet-filtered Navier–Stokes equations [29] showed that statistical predictability of isotropic turbulence can be preserved with a reduced number of degrees of freedom. This approach, called Coherent Vorticity Simulation (CVS) [14], is a multiscale method to compute incompressible turbulent flows based on the wavelet filtered vorticity field. The coherent vorticity, corresponding to the few coefficients whose modulus is larger than a threshold, represents the organized and energetic flow part, while the remaining incoherent vorticity is noise-like. Applying wavelet-based denoising, i.e., CVS filtering, to the 3D Galerkin truncated incompressible Euler equations confirmed that this adaptive regularization models turbulent dissipation and thus allows us to compute turbulent flows with intermittent nonlinear dynamics and a $k^{-5/3}$ Kolmogorov energy spectrum [13]. A significant compression rate of the wavelet coefficients of vorticity is likewise observed, which reduces the number of active degrees of freedom to only about 3.5% of the total number of coefficients for the studied turbulent flows, computed at a Taylor microscale-based Reynolds number of 200.

Filtering the wavelet representation of the Galerkin truncated inviscid Burgers and 2D incompressible Euler equations in [33], by retaining only the significant coefficients, showed that the spurious oscillations due to resonance can be filtered out, and dissipation can thus be introduced by the adaptive representation.

The aim of the current work is to provide a rigorous mathematical framework to analyze and to understand the properties of adaptive discretizations of evolutionary

PDEs based on dynamical Galerkin schemes. To this end we analyze these adaptive Galerkin discretizations. Galerkin schemes by themselves are particularly appealing due to their optimality properties, conservation of energy, and the ease of numerical analysis using Hilbert space techniques. Introducing space adaptivity, e.g., by wavelet filtering in each time step, implies that the projection operator changes over time as only a subset of basis functions is used. Hence, the projection operator is nondifferentiable in time, and we propose the use of an integral formulation. The projected equations are then analyzed with respect to existence and uniqueness of the solution. It is proven that nonsmooth projection operators introduce dissipation, a result which is crucial for adaptive discretizations of nonlinear PDEs. Existence and uniqueness of the solution of the projected equations is likewise shown. Tools from countable systems of ordinary differential equations and functional analysis in Banach spaces are used. For related background we refer the reader to the text books [11, 37] and [15].

The remainder of the article is organized as follows. Dynamical Galerkin schemes are defined in section 2, and the existence and uniqueness of the projected equations is analyzed, giving an explanation of the introduced energy dissipation. Space and time discretization of the Burgers and incompressible Euler equations is described in section 3. Numerical examples are presented in section 4 to illustrate the dissipation mechanism. Section 5 shows applications of the CVS filtering to the inviscid Burgers equation in 1D and the 2D and 3D incompressible Euler equations. Some conclusions are drawn in section 6.

2. Dynamical Galerkin schemes.

2.1. Motivation. Evolutionary PDEs can be discretized with a Galerkin method in space, by projecting the equation onto a sequence of finite dimensional linear spaces, which approximate the solution in space when the discretization parameter, h, goes to zero. Using truncation to a finite number of modes, the infinite dimensional countable system of ordinary differential equations in time can be reduced. An important restriction of such methods is that the projection space typically does not evolve in time and the number of modes is fixed. Here, we propose a formulation of adaptive Galerkin discretizations where the projection operator and the number of modes can change over time, and we show that under suitable conditions adaptation can introduce dissipation.

2.2. Formal definition. Let H be a Banach space, and consider the evolution equation

$$u' = f(u), \tag{2.1}$$

where u' denotes the weak time derivative of u and f is defined and continuous from some sub-Banach space $D(f) \subset H$ into H. Equation (2.1) is completed by a suitable initial condition $u(0) = u(t = 0)$. To be more specific, we shall focus below on the case of the one-dimensional Burgers equation on the torus $\mathbb{R}/\mathbb{Z}$:

$$\partial_t u + u\partial_x u = \nu \partial_{xx} u, \tag{2.2}$$

which corresponds to (2.1) with

$$f(u) = \nu \partial_{xx} u - u\partial_x u \tag{2.3}$$

and $u = u(x, t)$.

The classical Galerkin discretization of (2.1) is defined as follows: for $h > 0$, let H_h be a fixed finite dimensional subspace of $D(f)$, such that

$$\overline{\bigcup_{h>0} H_h} = H,$$

where the adherence is taken in H, and let P_h be the orthogonal projector on H_h. Find $u_h : [0,T] \in H_h$ such that

$$u_h' = P_h f(u_h) = P_h(\nu \partial_{xx} u_h - u_h \partial_x u_h). \tag{2.4}$$

Now for $t \in [0,T]$, assume that $P_h(t)$ is an orthogonal projector on some finite dimensional subspace $H_h(t)$ of H. The dimension of $H_h(t)$ is allowed to change in time, but we assume that $H_h(t)$ remains within a fixed finite dimensional subspace H_h^0. P_h therefore takes its values in the set of orthogonal projectors $H_h^0 \to H_h^0$, which we denote by Π_h^0, with its natural smooth manifold structure as a closed subset of all linear mappings $H_h^0 \to H_h^0$. We want to find $u_h : [0,T] \in H_h(t)$, which is an approximation of u.

Let us first assume that P_h is a smooth function of time. As in the case where P_h is time independent, we apply $P_h(t)$ to the differential equation to get

$$P_h(t) u_h'(t) = P_h(t) f(u_h(t)), \tag{2.5}$$

but now, since P_h does not commute with the time-derivative, this equation is not sufficient to determine $u_h'(t)$ entirely. We need another equation to fix the component of $u_h'(t)$ which is in the orthogonal of $H_h(t)$, i.e., in $H_h^\perp(t)$.

To derive this equation, we start from the condition that $u_h(t) \in H_h(t)$ for every t, which is equivalent to

$$P_h(t) u_h(t) = u_h(t). \tag{2.6}$$

Differentiating in time this identity leads to

$$P_h(t) u_h'(t) + P_h'(t) u_h = u_h'(t) \tag{2.7}$$

or, equivalently,

$$(1 - P_h(t))\, u_h'(t) = P_h'(t) u_h(t), \tag{2.8}$$

which is exactly the equation we were looking for. By adding (2.5) and (2.8) together, we obtain the definition of the dynamical Galerkin scheme:

$$u_h'(t) = P_h(t) f\left(u_h(t)\right) + P_h'(t) u_h(t). \tag{2.9}$$

By comparing this differential equation with (2.4), we observe the appearance of a new term proportional to the time-derivative of P_h. This is the essential ingredient that characterizes the dynamical Galerkin scheme. We now show the following lemma.

LEMMA 2.1. *Any solution of* (2.9) *such that* $u_h(0) \in H_h(0)$ *also satisfies* $u_h(t) \in H_h(t)$ *for all* t, *and moreover*

$$\frac{1}{2} \frac{\mathrm{d}}{\mathrm{d}t} \|u_h(t)\|^2 = (u_h(t), f(u_h(t))). \tag{2.10}$$

Proof. By differentiating $P_h(t)^2 = P_h(t)$ and $P_h(t)^3 = P_h(t)$, respectively, we obtain the identities

$$P_h(t)P_h(t)' + P_h(t)'P_h(t) = P_h(t)' \quad \text{and} \quad P_h(t)P_h(t)'P_h(t) = 0,$$

which imply that

$$\frac{\mathrm{d}}{\mathrm{d}t}\left((1 - P_h(t))u_h(t)\right) = 0, \tag{2.11}$$

and the first part follows. To prove the second part, take the inner product of the equation with u_h:

$$\frac{1}{2}\frac{\mathrm{d}}{\mathrm{d}t}\|u_h(t)\|^2 = (u_h(t), f(u_h(t))) + (u_h(t), P_h'(t)u_h(t)), \tag{2.12}$$

where the last term can be rewritten

$$(P_h(t)u_h(t), P_h'(t)P_h(t)u_h(t)) = (u_h(t), P_h(t)P_h'(t)P_h(t)u_h(t)) = 0,$$

which proves (2.10). ∎

The above computations are valid when P_h is differentiable, which is a severe restriction and forbids us in particular to switch on and off dynamically some functions in the basis of integration, which is the goal that we had set for ourselves in the beginning. To pursue this goal we therefore need to extend the definition of the scheme to nondifferentiable P_h. For this we consider the integral formulation of (2.9), namely

$$u_h(t) = u_h(0) + \int_0^t P_h(\tau)f(u_h(\tau))\mathrm{d}\tau + \int_0^t P_h'(\tau)u_h(\tau)\mathrm{d}\tau. \tag{2.13}$$

This equation can be rewritten using a Stieltjes integral with respect to P_h,

$$u_h(t) = u_h(0) + \int_0^t P_h(\tau)f(u_h(\tau))\mathrm{d}\tau + \int_0^t \mathrm{d}P_h(\tau)u_h(\tau), \tag{2.14}$$

which we call the integral formulation of the dynamical Galerkin scheme.

This equation makes sense as soon as P_h has bounded variation (BV), which gives it a much wider range of applicability than (2.9), allowing in particular discontinuities in P_h. To solve such an equation we need to resort to the theory of generalized ordinary differential equations, which we now recall.

2.3. Existence and uniqueness of a solution to the projected equations. The rigorous setting for integral equations such as (2.14) involving Stieltjes integrals is explained in detail in the book [37]. An alternative introduction can be found in [32]. We summarize the main consequences of the theory for our problem in the following theorem.

THEOREM 2.2. *Assume that $P_h(t) : [0, T] \to$ is BV and left-continuous, that $P_h(0)u_h(0) = u_h(0)$ (i.e., $u_h(0) \in H_h(0)$), and that $f : H_h^0 \to H$ is locally Lipschitz. Then*

(i) There exists T^*, $0 < T^* \leq T$, such that the integral equation

$$u_h(t) = u_h(0) + \int_0^t P_h(\tau)f(u_h(\tau))\mathrm{d}\tau + \int_0^t \mathrm{d}P_h(\tau)u_h(\tau) \tag{2.15}$$

has a unique BV, left-continuous solution $u_h : [0, T^*] \to H_h^0$.

(ii) This solution satisfies

$$\forall t \in [0,T], \quad P_h(t)u_h(t) = u_h(t). \tag{2.16}$$

(iii) u_h is continuous at any point of continuity of P_h, and more generally, for any t,

$$u_h(t^+) - u_h(t) = (P_h(t^+) - P_h(t))u_h(t) \tag{2.17}$$

or, equivalently,

$$u_h(t^+) = P_h(t^+)u_h(t). \tag{2.18}$$

(iv) The energy equation (2.10) for smooth P_h is replaced in general by

$$\begin{aligned} &\frac{1}{2}(\|u_h(t)\|^2 - \|u_h(0)\|^2) \\ &\quad = \int_0^t (u_h(\tau), f(u_h(\tau)))\mathrm{d}\tau - \frac{1}{2}\sum_{\{i|t_i<t\}} \|(1 - P_h(t_i^+))u_h(t_i)\|^2, \end{aligned} \tag{2.19}$$

where $(t_i)_{i\in\mathbb{N}}$ are the points of discontinuity of P_h.

Proof. To prove part (i) of the theorem we first need to familiarize ourselves with a few key concepts used by [37].

DEFINITION 2.3. *Let $G = \{x \in \mathbb{R}^n \mid \|x\| \le c\} \times [0,T]$, let $h : [0,T] \to \mathbb{R}$ be a nondecreasing, continuous from the left function, and let $\omega : [0,+\infty) \to \mathbb{R}$ be a continuous, increasing function with $\omega(0) = 0$.*

We will say that a function $F : G \to \mathbb{R}^n$ belongs to the class $\mathcal{F}(G,h,\omega)$ if and only if

$$\|F(x,t_2) - F(x,t_1)\| \le |h(t_2) - h(t_1)| \tag{2.20}$$

and

$$\|F(x,t_2) - F(x,t_1) - F(y,t_2) + F(y,t_1)\| \le \omega(\|x-y\|)|h(t_2) - h(t_1)| \tag{2.21}$$

for all $(x,t_2),(x,t_1),(y,t_2),(y,t_1) \in G$.

The proof of the existence is based on the Schauder–Tichonov fixed point theorem, using Theorem 4.2 on page 114 of [37]. The uniqueness can be shown using Theorem 4.8 on page 122 of [37] proving the local uniqueness property in the future, i.e., for increasing t.

Now let us turn to (ii). The idea is to approximate P_h by a family of smooth functions $P_{h,\varepsilon}$, $\varepsilon > 0$, and then to apply Lemma 2.1 to the corresponding solution $u_{h,\varepsilon}$, giving

$$(1 - P_{h,\varepsilon}(t))\ u_{h,\varepsilon}(t) = 0 \tag{2.22}$$

and then passing to the limit. For this we need $u_{h,\varepsilon}(t) \to u_h(t)$, which means that the solution depends continuously on P_h (see Chapter 8, page 262 of [37]: continuous dependence on parameters).

The continuity of u_h in part (iii) follows directly from the fact that P_h is left-continuous and BV.

The energy equation in part (iv) can be shown by integrating (2.12) in time and replacing $P_h'(t)u_h(t)$ by $(1-P_h(t))u_h'(t)$; cf. (2.8).

In the case when the projector $P_h(t)$ depends on $u(t)$, e.g., when using adaptive wavelet thresholding, we have

$$u_h(t) = u_h(0) + \int_0^t P_h(\tau) f(u_h(\tau)) \mathrm{d}\tau + \int_0^t \mathrm{d}P_h(\tau) u_h(\tau), \tag{2.23a}$$

$$P_h(t) = \Phi(u_h(t)). \tag{2.23b}$$

THEOREM 2.4. *Under certain conditions, the system* (2.23a) *has a unique solution.*

Proof. We proceed by iteration. Let P_h^0 be the projector on the time-independent approximation space H_h^0, and letu_h^0 be the corresponding solution of (2.23a). We then define recursively

$$P_h^{n+1}(t) = \Phi(u_h^n(t)) \tag{2.24}$$

and u_h^{n+1} as the solution of (2.23a) with $P_h = P_h^{n+1}$. ∎

3. Space and time discretization. For space discretization in the numerical results below we use a classical Fourier pseudo-spectral scheme [7]. The spectral Fourier projection of $u \in L^1(\mathbb{T}^d)$ where $\mathbb{T} = \mathbb{R}/(2\pi\mathbb{Z})$ is given by

$$P_N u(\boldsymbol{x}) = u_N(\boldsymbol{x}) = \sum_{|\boldsymbol{k}| \lesssim N/2} \widehat{u}_{\boldsymbol{k}}\, e^{i\boldsymbol{k}\cdot\boldsymbol{x}}\ ,\ \widehat{u}_{\boldsymbol{k}} = \frac{1}{(2\pi)^d} \int_{\mathbb{T}^d} u(\boldsymbol{x})\, e^{-i\boldsymbol{k}\cdot\boldsymbol{x}}\, d\boldsymbol{x}. \tag{3.1}$$

Note that $|k| \lesssim N/2$ is understood in the sense $-N/2 \le k < N/2$ and correspondingly in higher dimensions for each component of $\boldsymbol{k}$.

Applying the spectral discretization to the one-dimensional inviscid Burgers equation ($d = 1$),

$$\partial_t u + \frac{1}{2}\partial_x u^2 \ = \ 0 \quad \text{for} \quad x \in \mathbb{T} \quad \text{and} \quad t > 0 \tag{3.2}$$

with periodic boundary conditions and suitable initial condition $u(x, t = 0) = u_0(x)$ yields the Galerkin scheme

$$\partial_t u_N + \frac{1}{2}\partial_x \left(P_N (u_N)^2\right) \ = \ 0 \quad \text{for} \quad x \in \mathbb{T} \quad \text{and} \quad t > 0, \tag{3.3}$$

which corresponds to a nonlinear system of N coupled ODEs for $\widehat{u}_k(t)$ with $|k| \lesssim N/2$. A pseudo-spectral evaluation of the nonlinear term is utilized, and the product in physical space is fully dealiased. In other words, the Fourier modes retained in the expansion of the solution are such that $|k| \le k_C$, where k_C is the desired cut-off wave number, but the grid has $N = 3k_C$ points in each direction, versus $N = 2k_C$ for a nondealiased, critically sampled product. This dealiasing makes the pseudo-spectral scheme equivalent to a Fourier–Galerkin scheme up to round-off errors [7], and is thus conservative.

For the two- and three-dimensional incompressible Euler equations ($d = 2, 3$) with periodic boundary conditions,

$$\begin{aligned} \partial_t \boldsymbol{u} + (\boldsymbol{u}\cdot\nabla)\,\boldsymbol{u} &= -\nabla p \quad \text{for} \quad \boldsymbol{x} \in \mathbb{T}^d \quad \text{and} \quad t > 0, \\ \nabla\cdot\boldsymbol{u} &= 0, \end{aligned} \tag{3.4}$$

a similar spectral discretization can be applied. The pressure p is eliminated using the Leray projection onto divergence-free vector fields. Eventually a nonlinear system of coupled ODEs is obtained for the Fourier coefficients of the velocity $\widehat{\boldsymbol{u}}_{\boldsymbol{k}}(t)$.

For time discretization of the resulting ODE systems we stick to classical Runge–Kutta schemes, of order 4 for the 1D Burgers equation and the 3D Euler equations, while for 2D Euler 3rd order Runge–Kutta a low storage formulation is used; see [30], on page 20. For details on the convergence and stability of the above spectral schemes we refer the reader to [4]. Implementation features for the 1D Burgers equation and the 2D Euler equation can be found in [28] and [33]. For details on the scheme for 3D Euler we refer the reader to [13].

The Fourier space discretization described above could be replaced by any other Galerkin discretization, using, for instance, finite elements, or wavelets as basis functions. The interest of using wavelets is to introduce adaptive discretizations; see, e.g., [36, 12]. In this case the projector P is changing over time and is nonsmooth, which means that dissipation is introduced by removing/adding basis functions during the time stepping. This technique has been previously used for regularizing the Burgers equation and the incompressible Euler equations without a rigorous mathematical justification.

To test the influence of wavelet thresholding we introduce the concept of pseudo-adaptive simulations. The Fourier–Galerkin discretization is used to solve the PDE, but in each time step the numerical solution u_N is decomposed into a periodic orthogonal wavelet series of $L^2(\mathbb{T}^d)$. For $d = 1$ we thus have the 1D truncated wavelet series

$$P_J u_N(x) = u_N^J(x) = \overline{u}_{00} + \sum_{j=0}^{J-1} \sum_{i=0}^{2^j-1} \widetilde{u}_{ji} \psi_{ji}(x)\,, \quad \widetilde{u}_{ji} = \int_{\mathbb{T}} u_N(x) \psi_{ji}(x) dx, \tag{3.5}$$

where $\overline{u}_{00}$ is the mean value of the solution and $\widetilde{u}_{ji}$ are its wavelet coefficients. The wavelet $\psi_{ji}(x) = 2^{j/2}\psi(2^j x - i)$ quantifies fluctuations at scale 2^{-j} around position $i/2^j$ and $N = 2^J$ denotes the total number of grid points, corresponding to the finest resolution. Figure 1 illustrates Shannon and Meyer wavelets together with the corresponding Fourier transforms, which have compact support. This implies that both are trigonometric polynomials and can be spanned by a Fourier basis. For extensions to higher dimensions using tensor product constructions of wavelets, we refer the reader to [10]. From a computational point of view the additional cost of wavelet thresholding is negligible, as the fast wavelet transform has only $O(N)$ complexity, compared to $O(N \log N)$ for the fast Fourier transform used in the pseudo-spectral schemes.

Wavelet filtering, which is the basis of the Coherent Vorticity Simulation (CVS) [14], introduces a sparse representation of the solution by removing weak wavelet coefficients. Thresholding of the wavelet coefficients with a threshold ϵ, which typically depends on time, is performed. This yields a projection of the numerical solution u_N,

$$P_J^\epsilon u_N(x) = u_\epsilon^J(x) = \overline{u}_{00} + \sum_{j=0}^{J-1} \sum_{i=0}^{2^j-1} \rho_\epsilon\left(\widetilde{u}_{ji}\right) \psi_{ji}(x)\,, \tag{3.6}$$

where ρ_ϵ is the (hard) thresholding operator defined as

$$\rho_\epsilon(x) = \begin{cases} x & \text{for} \quad |x| > \epsilon, \\ 0 & \text{for} \quad |x| \le \epsilon, \end{cases} \tag{3.7}$$

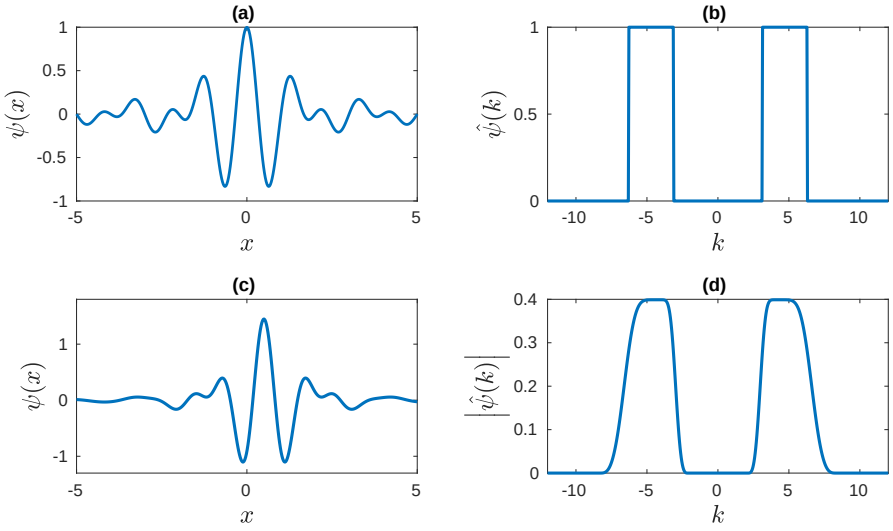

FIG. 1. *Shannon wavelet (top) and Meyer wavelet (bottom) in physical space $\psi(x)$ (left) and the corresponding modulus of the Fourier transform $|\widehat{\psi}(k)|$ (right).*

and ϵ denotes the threshold. The thresholding error can be estimated (see, e.g., [9]), and we have

$$||P_J u_N(x) - P_J^\epsilon u_N(x)||_2 \leq C\epsilon\,.$$

Using pseudo-adaptive simulations the CVS algorithm can be summarized as follows [33]:

(i) The Fourier coefficients of the solution $\widehat{u}_k$ for $|k| \lesssim N/2$ are advanced in time to $t = t_{n+1}$ and an inverse Fourier transform is applied on a grid of size N to obtain u_N.

(ii) A forward wavelet transform is performed to obtain $P_J u_N(x)$, according to (3.5).

(iii) CVS filtering removes wavelet coefficients having magnitude below the threshold ϵ. The threshold value is determined iteratively [1] and initialized with $\epsilon_0 = q\sqrt{||u||_2/2/N}$, where q is a compression parameter. The iteration steps are then obtained by $\epsilon_{s+1} = q\sigma[\widetilde{u}_{ji}^s]$ until $\epsilon_{s+1} = \epsilon_s$, where $\widetilde{u}_{ji}^s$ are the wavelet coefficients below ϵ_s and $\sigma[\cdot]$ is the standard deviation of the set of these coefficients.

(iv) A safety zone is added in wavelet space. The index set of retained wavelet coefficients in step iii) is denoted by Λ and for each retained wavelet coefficient indexed by $(j,i) \in \Lambda$ neighboring coefficients in position and scale (5 in the present case) are added, as illustrated in Figure 2.

(v) An inverse wavelet transform is applied to the wavelet coefficients above the final threshold, and a Fourier transform is then performed to obtain the Fourier coefficients of the filtered solution at time step t_{n+1}.

Different choices of the wavelet basis for regularization have been tested, e.g., in [33], including various orthogonal wavelets and a Dual-Tree Complex Wavelet basis we refer to as "Kingslets" [21]. The value of the compression parameter q controls the number of discarded coefficients, and in previous studies we found experimentally the

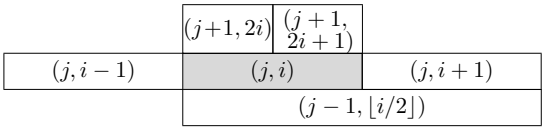

FIG. 2. *Safety zone in wavelet coefficient space around an active coefficient* (j, i) *in position* i *and finer* $(j + 1)$ *and coarser* $(j - 1)$ *scales.*

value $q = 5$ for "Kingslets" (complex-valued wavelets), and for orthogonal wavelets we used $q = 8$.

Adding a safety zone is necessary due to the lack of translational invariance of orthogonal wavelets, but also for local dealiasing. The idea is to keep neighboring coefficients in space and scale and to account for translation of shocks or step gradients and the generation of finer scale structures. For complex-valued wavelets, which are translation invariant, no safety zone is required, as shown in [33]. For details and further discussion on possible choices of the safety zone we refer the reader to [29].

4. Numerical experiments. In the following we show results to illustrate the properties of the dynamical Galerkin scheme and in particular their ability to introduce energy dissipation into the numerical method, which can be useful for stabilization. As examples we consider first the inviscid 1D Burgers equation using periodic boundary conditions. The initial condition is a simple sine wave given by $u(x, t = 0) = \sin(2\pi x)$ for $x \in \mathbb{T}$. Unless explicitly noted, computations are done with $N = 2048$ collocation points, and the time step Δt is chosen so that $\Delta x/\Delta t = 16$, where $\Delta x = 1/N$ is the grid discretization size. This choice ensures the CFL condition is met [7].

4.1. Punctual selection in the Fourier basis. The simplest illustration which we develop as a proof of concept is a punctual selection in the Fourier basis. Starting at some time instant t_b and during an entire interval $[t_b, t_e]$, we set to zero the Fourier coefficients corresponding to a given wave number k_f after each time step (both positive and negative modes are erased, such that the solution remains real). The projection operator thus becomes time dependent and discontinuous, and we have

$$P_N(t)^{k_f}_{[t_b,t_e]} u(x) = \begin{cases} \sum_{|k|\lesssim N/2, |k|\neq k_f} \widehat{u}_k \, e^{ik\,x} & \text{for} \quad t \in [t_b, t_e], \\ \sum_{|k|\lesssim N/2} \widehat{u}_k \, e^{ik\,x} & \text{elsewhere.} \end{cases} \tag{4.1}$$

The removal of these modes will instantly dissipate energy of the numerical solution, but from there on energy is conserved. And this is the case still after the reintroduction of the coefficients in the projection basis, despite the discontinuity of the projection operator. Indeed, according to (2.19) dissipation is observed as long as $\|(1 - P_h(t^+))u_h(t)\|^2$ is nonzero, but at $t = t_e$ this quantity is null, and therefore energy is conserved. We note that since a multistage time marching scheme is employed, it is necessary to reset to zero the removed coefficients after each substage to ensure they have no effect on the solution.

We show in Figure 3(a) the time evolution of the energy when the filtering wave number is $k_f = 2$. The projection operator changes at $t_b = 0.16$ and is then restored at $t_e = 0.2$. Dissipation is introduced by this change of projection basis and, up to numerical errors, the lost energy amounts to the energy content of the discarded

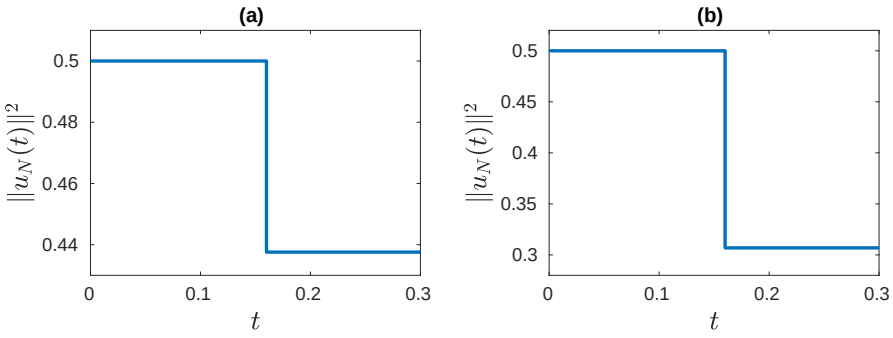

FIG. 3. *Filtering of one mode in* (a) *Fourier space and* (b) *wavelet space for the inviscid* 1*D Burgers equation. Time evolution of energy. As expected, energy loss is observed.*

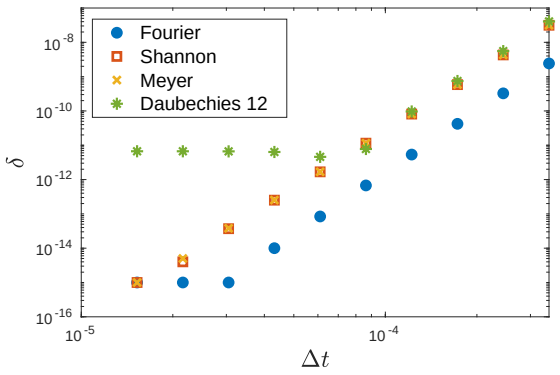

FIG. 4. *Difference between dissipated energy and filtered energy (equation* (4.2)*) as a function of the time step* Δt*, when a single Fourier mode or wavelet coefficient is filtered. A residual difference remains when Daubechies wavelets are employed.*

coefficients. This can be seen in Figure 4, where we plot, as a function of the time step Δt, the quantity

$$\delta = (\|u_N(0)\|^2 - \|u_N(t_b)\|^2) - \|(1 - P_N(t_b^+)_{[t_b,t_e]}^{k_f})u_N(t_b)\|^2, \tag{4.2}$$

which should be zero according to (2.19), since the PDE is energy conserving up to time t_b. One observes that δ indeed converges to zero up to machine precision (of order 10^{-15}) as Δt is decreased. It is interesting to mention that the method developed in [26] employs a punctual periodic filtering in Fourier space to regularize solutions of the inviscid Burgers equation, so the above discussion formalizes the dissipation step used there.

4.2. Punctual selection in real orthogonal wavelet bases. To illustrate dissipation through reprojection on a wavelet basis, we extend the previous idea of a punctual selection now to wavelet space. The solution of the Fourier–Galerkin method is decomposed in each time step into an orthogonal wavelet basis, as in (3.5). One single energy containing coefficient, of scale index j_f and position index i_f, is then set to zero after every time step during some given time interval $[t_b, t_e]$. The projection operator is once again time dependent and discontinuous and may be written as

(4.3)
$$P_J(t)^{j_f,i_f}_{[t_b,t_e]}u(x) = \begin{cases} \overline{u}_{00} + \sum_{j=0}^{J-1}\sum_{i=0}^{2^j-1} \widetilde{u}_{ji}\psi_{ji}(x)(1-\delta_{jj_f}\delta_{ii_f}) & \text{for} \quad t \in [t_b, t_e], \\ \overline{u}_{00} + \sum_{j=0}^{J-1}\sum_{i=0}^{2^j-1} \widetilde{u}_{ji}\psi_{ji}(x) & \text{elsewhere} \end{cases}$$

for a chosen orthogonal wavelet $\psi_{ji}(x)$.

We show in Figure 3(b) the energy time evolution for the case of projections in the Meyer wavelet basis. The filtered coefficient corresponds to $j_f = 1$ and $i_f = 1$. As before, the filtering happens from time $t_b = 0.16$ to $t_e = 0.2$. Energy is punctually dissipated as of the first change in the projector, but is otherwise conserved. Figure 4 also shows the convergence of the quantity δ from (4.2), now with the projector replaced by (4.3). Similar results are also obtained with projections onto a Shannon wavelet basis.

Interestingly, the same convergence is not observed in Figure 4 when Daubechies wavelets are used. As illustrated in Figure 1, working with Shannon wavelets is actually equivalent to working with the Fourier basis, since it is compactly supported in spectral space, with a sharp cut-off. Combining multiscale Shannon wavelets amounts to covering the spectral space up to some Galerkin cut-off frequency. When projecting with this basis, one is simply damping some existing Fourier coefficients without introducing new wave numbers. Hence, when going back to the fully dealiased Fourier space, no further energy is lost. The Meyer wavelet is likewise compactly supported in spectral space; however, the projection onto Meyer wavelets is only equivalent to a Fourier projection when the number of Fourier modes is increased from N to $3/2N$, which is the case when dealiasing is applied. Therefore, in both cases the dissipated energy indeed corresponds to the energy lost due to the discontinuity of the projection operator. The Daubechies wavelet, on the other hand, is not compactly supported in spectral space. When a projection is made in wavelet space and some coefficient is discarded, this will affect wave numbers beyond the dealiased ones, which then cease to vanish. After returning to Fourier space, the dealiasing operation will set all these to zero, and further energy dissipation occurs. For this reason, the quantity δ shows a residual value as the time step decreases and does not attain machine precision, as seen in Figure 4. In this simulation, Daubechies 12 wavelets were employed and the projector corresponds to (4.3) with $j_f = 0$ and $i_f = 0$. Note that the indices are chosen so that the amount of dissipated energy is comparable in all cases.

This additional energy dissipation can once again be understood as due to a change in the projector, i.e., going from the wavelet projector removing one coefficient, given in (4.3), to the Fourier projector given in (3.1). In other words, it is the fact that these two projectors do not commute when Daubechies wavelets are used (or any other basis not compactly supported in Fourier space, i.e., within the fully dealiased spectral space) which leads to more dissipation than that introduced by the filtering. This shows that pseudo-adaptive simulations, such as those discussed in section 3, must be interpreted with care, since they may not exactly reproduce what one would get with a fully adaptive scheme in wavelet space. Still, they are valuable tools to predict the solutions'; behavior in a simpler and faster setup, and we shall apply them to illustrate the introduction of dissipation in conservation laws through a dynamical Galerkin scheme.

5. Application to the inviscid Burgers equation and incompressible Euler using CVS filtering. In the following section we present in a concise way some results from the literature to illustrate the dissipation properties of adaptive

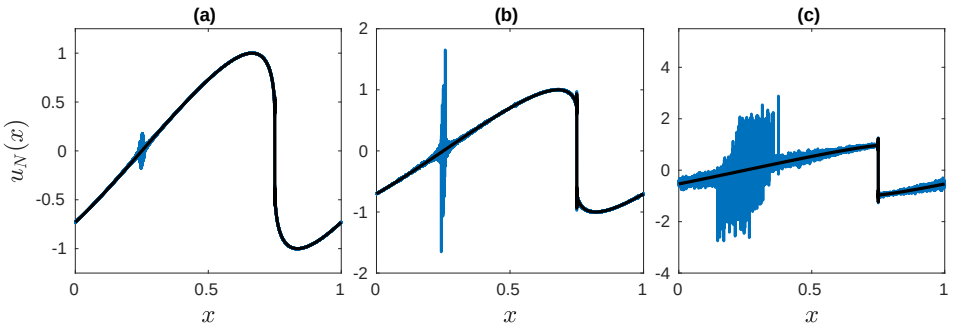

FIG. 5. *CVS-filtered Galerkin truncated inviscid Burgers equation using complex-valued wavelets (Kingslets, in black) together with the nondissipative Galerkin truncated solution (blue) at times* $t = 0.1644$, 0.1793, *and* 0.3. *The solutions are periodically shifted to the right, so that both the resonances and the shocks can be easily seen.*

Galerkin methods using CVS filtering. We show some numerical examples for the 1D inviscid Burgers equation including some space-time convergence and for the incompressible Euler equations in two and three dimensions. For details on the numerical simulations we refer the reader to [33] and [13].

5.1. Inviscid Burgers. We consider the inviscid Burgers equation (3.2), discretized with a Fourier pseudo-spectral method and endowed with CVS filtering, described in section 3, using $N = 16384$ Fourier modes. For the used sinusoidal initial condition $u(x, t = 0) = \sin(2\pi t)$ the time evolution of the reference solution, the so-called entropy solution, can be easily computed with the method of characteristics, separately in each half of the domain. Figure 5 shows the solution of the standard Fourier–Galerkin method, which preserves energy, and the solution obtained with the dynamic Galerkin scheme using CVS filtering with "Kingslets." We observe that the oscillations (also called resonances; see [34]), which appear as soon as the shock is formed, are removed using CVS filtering. This is further confirmed in Figure 7 (left), where the oscillations are shown to be completely filtered out and a smooth solution close to the reference solution is obtained.

To assess the filtering performance, we develop a space-time convergence analysis by computing the time integrated relative L^2-distance from the filtered solution u_N to the analytical reference solution u_{ref}. We compute

$$\mathcal{E} = \int_{t_0}^{t_1} \frac{\|u_N(t) - u_{\mathrm{ref}}(t)\|^2}{\|u_{\mathrm{ref}}(t)\|^2} dt \tag{5.1}$$

for different space resolutions while keeping fixed the previous relation between time and space discretization, that is, $\Delta x/\Delta t = 16$. Since the filtering is only relevant after the shock formation, we actually start the analysis from a time right before the shock time $t_s = \inf_x [-1/u'(x, 0)] \approx 0.1592$, i.e., $t_0 = t_s - \Delta t$, and carry out the integration up to $t_1 = 0.3$. Results for complex-valued Kingslets and real-valued Shannon wavelets with and without the safety zone discussed in section 3 are shown in Figure 6. We can observe that CVS with Kingslets is in excellent agreement with the reference solution, showing an $\mathcal{O}(\Delta x)$ convergence rate. Although typically one order of magnitude poorer (an underperformance that we now quantify but which has only been visually verified in [33]), CVS with Shannon wavelets also shows first order convergence towards the reference solution if the safety zone is present. We note

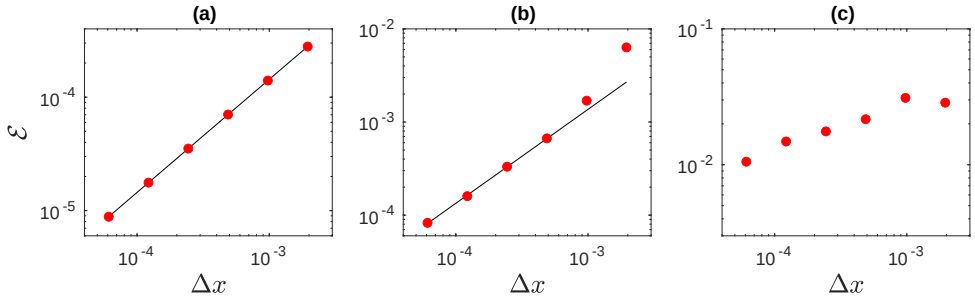

FIG. 6. *Time integrated relative L^2-error (equation (5.1)) as a function of space resolution Δx.* (a) *Kingslets.* (b) *Shannon wavelet with the safety zone.* (c) *Shannon wavelet without the safety zone. The straight lines have slope* 1.

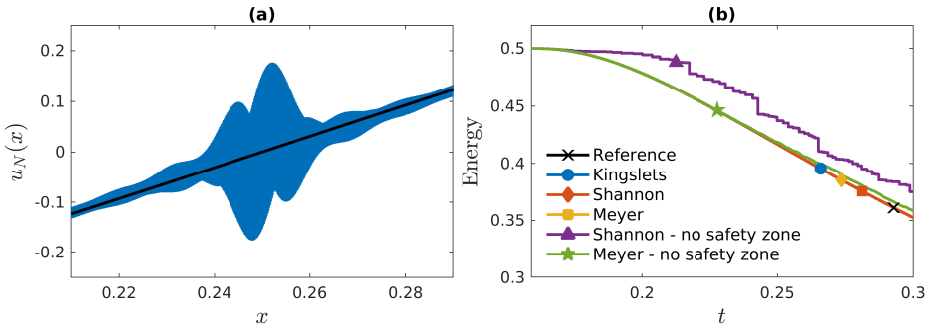

FIG. 7. (a) *Detail of the solution of CVS-filtered Galerkin truncated inviscid Burgers equation using complex-valued wavelets (Kingslets, in black) together with the nondissipative Galerkin truncated solution (blue) at time* $t = 0.1644$. (b) *Time evolution of the energy $E(t)$ of CVS filtered solutions for different wavelets with and without safety zone together with the analytical result.*

that this is the same convergence rate observed with the periodic Fourier filtering of [26]. In comparison to this method, CVS has the disadvantage of being less simply implemented but offers the attractive feature of compression, with only a very reduced number of degrees of freedom being necessary to reproduce the physical reference solution. Meanwhile, as anticipated in section 3, Figure 6(c) shows that CVS is not able to properly regularize the solution when employing real orthogonal wavelets if a safety zone is not introduced.

The evolution of the energy $E = \frac{1}{2}||u||^2$ shown in Figure 7 (right) further quantifies the dissipation of the adaptive schemes for different real orthogonal wavelets. Once again, in the presence of the safety zone the wavelet adaptation removes sufficient energy, matching thus the analytical energy evolution. However, it is now seen that without the safety zone not enough energy is dissipated and the solution is not properly regularized. For a detailed description of similar simulations and a physical interpretation we refer to [33].

5.2. Incompressible Euler equations. To illustrate the effect of dissipation when adapting the basis functions using projectors changing over time we consider the incompressible Euler equations given in (3.4) and discretize them with a classical Fourier–Galerkin scheme. In these pseudo-adaptive simulations we apply in each time

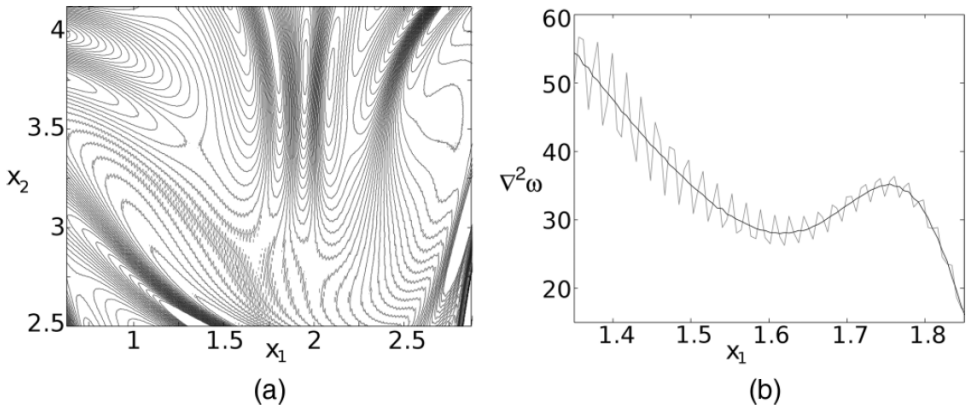

FIG. 8. *Filtering of 2D incompressible Euler using complex-valued wavelets (Kingslets). Left: Contours of the Laplacian of vorticity $\Delta\omega$ at $t = 0.71$. The Galerkin truncated solution is shown in gray, and the CVS solution is given in black. Right: 1D cut of the Laplacian of vorticity for the oscillatory Galerkin truncated solution and the wavelet-filtered smooth solution. Reprinted with permission from Phys. Rev. E,* 87 *(*2013*),* 033017*,* https:doi.org/10.1103/PhysRevE.87.033017*. Copyright (*2013*) by the American Physical Society.*

step CVS filtering. Detailed results can be found in [33] and [13] for the 2D and 3D cases, respectively.

In the 2D case a random initial condition is evolved in time with third order Runge–Kutta time integration using a resolution of $N = 1024^2$ Fourier modes [33]. Visualizations of the Laplacian of vorticity $\omega = \nabla \times \boldsymbol{u}$ in the fully developed nonlinear regime are shown in Figure 8 (left). For the Galerkin truncated solution we find oscillations in the isolines in $\Delta\omega$ (a small scale quantity, which is sensitive to oscillations), while the regularized solution using complex-valued wavelets with CVS filtering yields a smooth solution. A 1D cut in Figure 8 (right) illustrates that in the CVS solution the oscillations have been indeed removed. In Figure 9, time evolution of enstrophy, defined as $\frac{1}{2}||\omega||_2^2$, shows that in contrast to the Galerkin truncated simulation the CVS computation is dissipative, and the enstrophy departs from the one of the conservative Galerkin truncated case, and it decays for times larger than 1.4. For more details, including a physical interpretation, we refer the reader to [33].

The 3D Fourier–Galerkin computations of incompressible Euler have been performed at resolution $N = 512^3$ in a periodic cubic domain with a fourth order Runge–Kutta scheme for time integration [13]. A statistically stationary flow of fully developed homogeneous isotropic turbulence obtained by DNS is used as the initial condition. For CVS filtering Coiflet 12 wavelets [10] were used. Note that the wavelet decomposition and subsequent filtering have been applied to the vorticity $\boldsymbol{\omega} = \nabla \times \boldsymbol{u}$ (and not to the velocity $\boldsymbol{u}$) in each time step, and subsequently the filtered velocity has been computed by applying the Biot–Savart operator $(\nabla\times)^{-1}$ in Fourier space.

The time evolution of the energy, $\frac{1}{2}||\boldsymbol{u}||_2^2$, and enstrophy, $\frac{1}{2}||\boldsymbol{\omega}||_2^2$, in Figure 10 first shows that the Galerkin truncted Euler computation preserves energy and that enstrophy grows rapidly in time due to the absence of regularization. For CVS we can observe that energy is dissipated, similar to what is observed for Navier–Stokes and that enstrophy also exhibits a similar evolution as Navier–Stokes and does not grow rapidly.

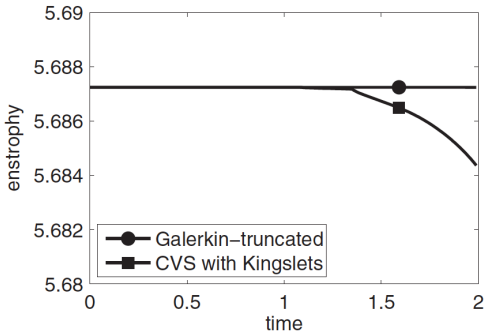

FIG. 9. *Filtering of 2D incompressible Euler using complex-valued wavelets (Kingslets). Evolution of enstrophy* $1/2||\omega||_2^2$ *for the Galerkin truncated case and the adaptive wavelet filtered case using Kingslets. Reprinted with permission from Phys. Rev. E,* 87 *(*2013*),* 033017, https:doi.org/10.1103/PhysRevE.87.033017. *Copyright (*2013*) by the American Physical Society.*

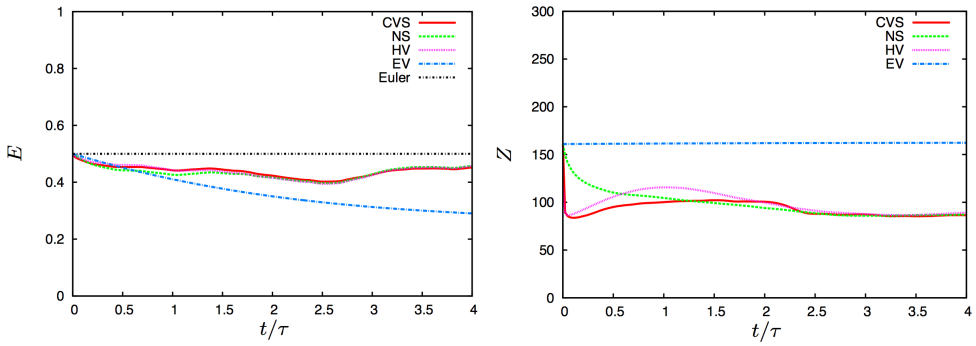

FIG. 10. *Energy (left) and enstrophy (right) evolution for 3D incompressible Euler using for Galerkin truncated Euler (Euler), wavelet filtered Euler (CVS), and Navier–Stokes (NS). HV and EV stand for hyperviscous regularization and Euler–Voigt, respectively, which are not discussed here. Reprinted with permission from Phys. Rev. E,* 96 *(*2017*),* 063119, https://doi.org/10.1103/PhysRevE.96.063119. *Copyright (*2017*) by the American Physical Society.*

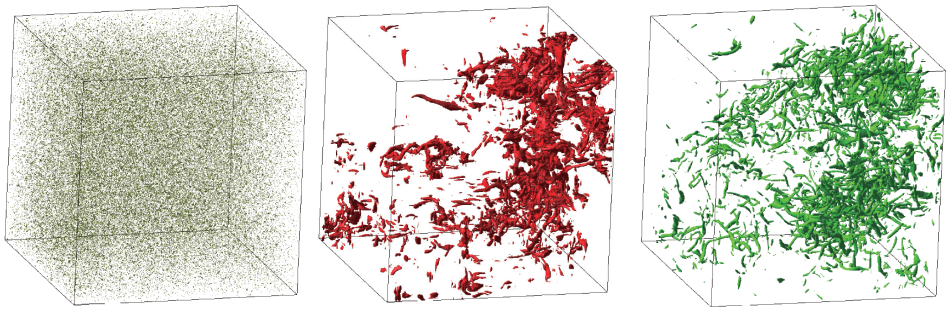

FIG. 11. *Vorticity isosurfaces,* $|\boldsymbol{\omega}| = M + 4\sigma$ *(where* M *is the mean value and* σ *the standard deviation of the modulus of vorticity of NS) for 3D incompressible Euler using Galerkin truncated Euler (Euler, left), wavelet filtered Euler (CVS, center), and Navier–Stokes (NS, right) at time* $t/\tau = 3.4$. *Reprinted with permission from Phys. Rev. E,* 96 *(*2017*),* 063119, https://doi.org/10.1103/PhysRevE.96.063119. *Copyright (*2017*) by the American Physical Society.*

Visualizations of intense vorticity structures in Figure 11 for CVS and Navier–Stokes show their similar tube-like character, while the Galerkin truncated Euler solution is similar to Gaussian white noise without the presence of coherent structures. For details, including a physical interpretation of the results, we refer the reader to [13].

6. Conclusions. We presented a mathematical framework for analyzing dynamical Galerkin discretizations of evolutionary PDEs. The concept of weak formulations of countable ODEs with nonsmooth right-hand side in Banach spaces is used. We showed that changing the set of active basis functions, which implies that the projection operators are nondifferentiable in time, can introduce energy dissipation. This feature is of crucial interest for adaptive schemes for time dependent equations, e.g., adaptive wavelet schemes for hyperbolic conservation laws, and yields a mathematical explanation for their regularizing properties due to dissipation.

Numerical experiments illustrated the above results for the inviscid Burgers equation and the incompressible Euler equations in two and three space dimensions. To this end the concept of pseudo-adaptive simulations was introduced to test the influence of wavelet thresholding, while solving the PDE with the classical Fourier Galerkin discretization. The results showed that adaptive wavelet-based regularization (i.e., filtering out the weak wavelet coefficients) of Galerkin schemes introduce dissipation together with related space adaptivity. The latter can be used for reducing the computational cost in fully adaptive computations. Moreover for the 1D Burgers equation we showed convergence towards the entropy solution. For the 2D and 3D Euler equations we found that oscillations present in the Galerkin truncated case are removed and energy is dissipated. However, for 2D and 3D Euler in general no exact reference solutions are available, and further analyses are necessary, which are left for future work. Finally, let us mention that an interesting link exists with LES models (see e.g., [35]), as the equivalence between nonlinear wavelet thresholding (using Haar wavelets) and a single step of explicitly discretized nonlinear diffusion can be shown; see [25].

This work opens some perspectives for the systematic studies of nonlinear hyperbolic conservation laws using adaptive Galerkin discretizations, in particular wavelet-based schemes and their regularization properties introducing viscous dissipation. In particular, it would be interesting to analyze whether the proposed wavelet filtering scheme is also able to handle the oscillations observed in the hyperviscous case [17, 2], which are due to bottlenecks in the energy spectrum and have a different nature than those due to the Galerkin truncation of the inviscid equations.

Acknowledgment. The authors would like to thank Greg Hammett for a discussion which strongly motivated this work. NVY thanks the Humboldt Foundation for post-doctoral support.

REFERENCES

[1] A. Azzalini, M. Farge, and K. Schneider, *Nonlinear wavelet thresholding: A recursive method to determine the optimal denoising threshold*, Appl. Comput. Harmon. Anal., 18 (2005), pp. 177–185.

[2] D. Banerjee and S. S. Ray, *Transition from dissipative to conservative dynamics in equations of hydrodynamics*, Phys. Rev. E, 90 (2014), 041001.

[3] C. Bardos, J. S. Linshiz, and E. S. Titi, *Global regularity for a Birkhoff-Rott-α approximation of the dynamics of vortex sheets of the 2d Euler equations*, Phys. D Nonlinear Phenom., 237 (2008), pp. 1905–1911.

[4] C. Bardos and E. Tadmor, *Stability and spectral convergence of Fourier method for nonlinear problems: On the shortcomings of the* 2/3 *de-aliasing method*, Numer. Math., 129 (2013), pp. 749–782.
[5] C. Basdevant, B. Legras, R. Sadourny, and M. Béland, *A study of barotropic model flows: Intermittency, waves and predictability*, J. Atmos. Sci., 38 (1981), pp. 2305–2326.
[6] A. Brandt, *Multi-level adaptive solutions to boundary-value problems*, Math. Comp., 31 (1977), pp. 333–390.
[7] C. Canuto, A. Quarteroni, M. Y. Hussaini, and T. A. Zang, *Spectral Methods in Fluid Dynamics*, Springer-Verlag, New York, 1988.
[8] C. Cichowlas, P. Bonaïti, F. Debbasch, and M. Brachet, *Effective dissipation and turbulence in spectrally truncated Euler flows*, Phys. Rev. Lett., 95 (2005), 264502.
[9] A. Cohen, *Wavelet methods in numerical analysis*, in Handbook of Numerical Analysis, Vol. VII, P. G.Ciarlet and J. L.Lions, eds., North-Holland, Amsterdam, 2000.
[10] I. Daubechies , *Ten Lectures on Wavelets*, CBMS-NSF Res. Conf. Ser. Appl. Math. 61, SIAM, Philadelphia, 1992, https://doi.org/10.1137/1.9781611970104.
[11] K. Deimling, *Ordinary Differential Equations in Banach Spaces*, Springer, New York, 1977.
[12] T. Engels, K. Schneider, J. Reiss, and M. Farge, *A wavelet adaptive method for multiscale simulation of turbulent flows in flying insects*, Commun. Comput. Phys., 30 (2021), pp. 1118–1149.
[13] M. Farge, N. Okamoto, K. Schneider, and K. Yoshimatsu, *Wavelet-based regularization of the Galerkin truncated three-dimensional incompressible Euler flows*, Phys. Rev. E, 96 (2017), 063119.
[14] M. Farge, K. Schneider, and N. Kevlahan, *Non-Gaussianity and coherent vortex simulation for two-dimensional turbulence using an adaptive orthogonal wavelet basis*, Phys. Fluids, 11 (1999), pp. 2187–2201.
[15] A. F. Filippov, *Differential Equations with Discontinuous Right Hand Sides*, Math. Appl. 18, Springer, Dordrecht, The Netherlands, 2013.
[16] U. Frisch, S. Kurien, R. Pandit, W. Pauls, S. S. Ray, A. Wirth, and J. Z. Zhu, *Hyperviscosity, Galerkin truncation, and bottlenecks in turbulence*, Phys. Rev. Lett., 101 (2008), 144501.
[17] U. Frisch, S. S. Ray, G. Sahoo, D. Banerjee, and R. Pandit, *Real-space manifestations of bottlenecks in turbulence spectra*, Phys. Rev. Lett., 110 (2013), 064501.
[18] D. Gottlieb and J. S. Hesthaven, *Spectral methods for hyperbolic problems*, J. Comput. Appl. Math., 128 (2001), pp. 83–131.
[19] A. Harten, *High resolution schemes for hyperbolic conservation laws*, J. Comput. Phys., 49 (1983), pp. 357–393.
[20] T. Ishihara, T. Gotoh, and Y. Kaneda, *Study of high-Reynolds number isotropic turbulence by direct numerical simulation*, Annu. Rev. Fluid Mech., 41 (2009), pp. 165–180.
[21] N. Kingsbury, *Complex wavelets for shift invariant analysis and filtering of signals*, Appl. Comput. Harmon. Anal., 10 (2001), pp. 234–253.
[22] B. Khouider and E. S. Titi, *An inviscid regularization for the surface quasi-geostrophic equation*, Commun. Pure Appl. Math., 61 (2008), pp. 1331–1346.
[23] T. D. Lee, *On some statistical properties of hydrodynamical and magneto-hydrodynamical fields*, Quart. Appl. Math., 10 (1952), pp. 69–74.
[24] A. Majda and I. Timofeyev, *Remarkable statistical behavior for truncated Burgers-Hopf dynamics*, Proc. Natl. Acad. Sci. USA, 97 (2000), pp. 12413–12417.
[25] P. Mrázek, J. Weickert, and G. Steidl, *Correspondences between wavelet shrinkage and nonlinear diffusion*, in Scale-Space 2003, L. D.Griffinand and M.Lillholm,eds., Lecture Notes in Comput. Sci. 2695, Springer, Berlin, 2003, pp. 101–116.
[26] S. D. Murugan, U. Frisch, S. Nazarenko, N. Besse, and S. S. Ray, *Suppressing thermalization and constructing weak solutions in truncated inviscid equations of hydrodynamics: lessons from the Burgers equation*, Phys. Rev. Res., 2 (2020), 033202.
[27] R. Nguyen van yen, M. Farge, D. Kolomenskiy, K. Schneider, and N. Kingsbury, *Wavelets meet Burgulence: CVS-filtered Burgers equation*, Phys. D Nonlinear Phenom., 237 (2008), pp. 2151–2157.
[28] R. Nguyen van yen, M. Farge, and K. Schneider, *Wavelet regularization of a Fourier-Galerkin method for solving the* 2*D incompressible Euler equations*, ESAIM Proc., 29 (2009), pp. 89–107.
[29] N. Okamoto, K. Yoshimatsu, K. Schneider, M. Farge, and Y. Kaneda, *Coherent vortex simulation of three-dimensional decaying homogeneous isotropic turbulence*, Multiscale Model. Simul., 9 (2011), pp. 1144–1161, https://doi.org/10.1137/10079598X.

[30] P. Orlandi, *Fluid Flow Phenomena: A Numerical Toolkit*, Springer, New York, 2000.
[31] S. Osher and F. Solomon, *Upwind difference schemes for hyperbolic systems of conservation laws*, Math. Comput., 38 (1982), pp. 339–374.
[32] S. G. Pandit and S. G. Deo , *Differential Equations Involving Impulses*, Lecture Notes in Math. 954, Springer, New York, 1982.
[33] R. M. Pereira, R. Nguyen van yen, M. Farge, and K. Schneider, *Wavelet methods to eliminate resonances in the Galerkin-truncated Burgers and Euler equations*, Phys. Rev. E, 87 (2013), 033017.
[34] S. S. Ray, U. Frisch, S. Nazarenko, and T. Matsumuto, *Resonance phenomenon for the Galerkin-truncated Burgers and Euler equations*, Phys. Rev. E, 84 (2011), 016301.
[35] K. Schneider, J. Ziuber, M. Farge, and A. Azzalini, *Coherent vortex extraction and simulation of 2D isotropic turbulence*, J. Turbul., 7 (2006), 44.
[36] K. Schneider and O. Vasilyev, *Wavelet methods in computational fluid dynamics*, Annu. Rev. Fluid Mech., 42 (2010), pp. 473–503.
[37] S. Schwabik, *Generalized Ordinary Differential Equations*, Ser. Real Anal. 5, World Scientific, River Edge, NJ, 1992.
[38] P. K. Sweby, *High resolution schemes using flux limiters for hyperbolic conservation laws*, SIAM J. Numer. Anal., 21 (1984), pp. 995–1011, https://doi.org/10.1137/0721062.
[39] E. Tadmor, *Convergence of spectral methods for nonlinear conservation laws*, SIAM J. Numer. Anal., 26 (1989), pp. 30–44, https://doi.org/10.1137/0726003.
[40] M. Vergassola, B. Dubrulle, U. Frisch, and A. Noullez, *Burgers' equation, devil's staircases and the mass distribution for large-scale structures*, Astron. Astrophys., 289 (1994), pp. 325–356.